Fingering instability transition in radially tapered Hele-Shaw cells: Insights at the onset of nonlinear effects

Pedro H. A. Anjos, Eduardo O. Dias,* and José A. Miranda†
Departamento de Física, Universidade Federal de Pernambuco, Recife, Pernambuco 50670-901, Brazil

(Received 13 April 2018; published 28 December 2018)

We investigate the effect of the capillary number Ca on the interfacial viscous fingering instability in radially tapered Hele-Shaw cells. By employing a perturbative weakly nonlinear approach, we manage to identify a fingering instability transition in the system at the onset of nonlinearities. We find that for low Ca the interface in tapered situations is stabilized (destabilized) in converging (diverging) cells, with respect to the equivalent behavior occurring in a parallel-plate (uniform) Hele-Shaw cell. However, for large Ca, we observe that the relative stability behavior changes, so that converging cells destabilize the interface in comparison to uniform cells, while diverging cells lead to relatively more stable interfaces. Moreover, we verify that finger tip-splitting is favored for large Ca, and restrained in the low-Ca regime. Our weakly nonlinear results are qualitatively consistent with recent intensive numerical simulations in the literature in which such an instability transition was examined at fully nonlinear stages of the flow.

DOI: 10.1103/PhysRevFluids.3.124004

I. INTRODUCTION

The viscous fingering instability has received a great deal of attention since the seminal work of Saffman and Taylor [1], and has become a well-known paradigm of interfacial pattern formation [2,3]. This hydrodynamic instability occurs when a fluid displaces another of larger viscosity in the narrow gap separating two parallel glass plates of a Hele-Shaw cell [4]. Ordinarily, the fluids are Newtonian and immiscible. Under such conditions, the fluid-fluid interface is unstable and develops into a variety of pattern-forming structures. In rectangular (rectilinear channel-shaped) Hele-Shaw cells [5–8] the resulting fingers are usually steady state, long and smooth. In contrast, in radial (circular) Hele-Shaw flows [9–12] highly ramified morphologies are observed during multiple stages of instability, where the evolving fingers tend to split at their tips, leading to the emergence of characteristic finger-tip-splitting phenomena. In the framework of the classic Saffman-Taylor problem, there is no instability when a more viscous fluid displaces a less viscous one, constituting a stable, reverse flow displacement. In this situation, the two-fluid boundary remains flat for rectangular flows and grows axisymmetrically as a perfect circle in radial Hele-Shaw cells.

Over the past several decades researchers have analyzed the effects of a number of variations of the traditional Saffman-Taylor setup. Among many other interesting modifications, studies include the incorporation of non-Newtonian [13–15], miscible [16–18], and reactive [19–21] fluids, the presence of magnetic fields acting on magnetic liquids (ferrofluids) [22–24], the influence of centrifugal and Coriolis forces on rotating Hele-Shaw cells [25–28], the impact of fluid inertia [29–31] and wetting effects [32–34], as well as the consideration of fluid displacements in curved (cylindrical, spherical, Gaussian profile shaped, etc.) Hele-Shaw cells [35–37]. Among all these

*eduardodias@df.ufpe.br
†jme@df.ufpe.br

different possibilities, there has been a growing interest in a particular alteration of the conventional viscous fingering problem that considers the situation in which the Hele-Shaw cell plates are no longer parallel. This specific modification was introduced some time ago by Zhao *et al.* [38] who added a small gradient in the gap of an originally parallel-plate rectangular Hele-Shaw cell. Their main goal was to understand the effect of such variable gap thickness both on the stability and shape of the produced interfacial fingers. In this tapered Hele-Shaw geometry, the small gap gradient can be either positive (slowly diverging plates) or negative (gently converging plates).

By performing laboratory experiments and linear stability analysis, Zhao *et al.* [38] focused on the high-capillary-number regime, where the capillary number Ca measures the relative strength of viscous to surface tension forces. Their linear stability results indicate that the small gap gradient has a negligible effect on the early stage pattern formation. However, their experimental findings reveal just the opposite, showing that the sign of the gap gradient strongly affects the finger-tip behavior: a positive gradient produces wide fingers which become susceptible to the tip-splitting instability, and negative gradients result in narrower fingers that are more stable than their parallel-plate cell counterparts. Later Dias and Miranda [39] succeeded to predict the experimental results observed in Ref. [38] for the case of high capillary numbers by carrying out an analytical weakly nonlinear analysis of the tapered rectangular flow problem.

In contrast to what has been done in Refs. [38,39], Al-Housseiny *et al.* [40] concentrated their attention on the low-capillary-number regime, and used linear stability analysis and experiments to unveil a new facet of the small-gap-gradient problem in rectangular Hele-Shaw cell geometry [41,42]. The investigations performed in Ref. [40] have demonstrated that the introduction of the small gap gradient can indeed be utilized to control the development of the viscous fingering instability. In other words, the gap gradient can either cause the entire suppression of the usual viscous fingering instability, or it can trigger the instability even under traditionally stable reverse flow circumstances.

In fact, the theoretical and experimental studies presented in Refs. [38–40] established that a small gap gradient may profoundly impact the behavior of the fluid-fluid interface in rectangular Hele-Shaw flows: in the high-Ca regime the gap gradient can determine the shape of the finger tip (wider or narrower than the conventional parallel-plate behavior), while in the low-Ca regime the gap gradient can be used to tune the occurrence of the Saffman-Taylor instability (either by restraining its emergence, or by stimulating its appearance under usually stable conditions).

Unlike the case of rectangular Hele-Shaw flows, for which the role of a small gap gradient was investigated using both theory (linear and weakly nonlinear analyses) and experiments, the corresponding scenario for flows in radially tapered Hele-Shaw cells is a bit different. The existing tapered radial flow studies are mostly restricted to theoretical explorations, i.e., the study of the onset of the viscous fingering instability through analytical linear stability analysis [43], or the examination of the fully nonlinear stages of interfacial evolution via intensive numerical simulations [44]. The linear stability analysis executed in Ref. [43] finds that at early linear stages of the flow in radially diverging cells the fluid-fluid interface is initially slowed down but eventually destabilizes as time progresses. Additionally, they have verified that for converging Hele-Shaw cells, the development of viscous fingering can be completely suppressed. As reported in Ref. [43], experiments considering the action of a small gap gradient in radial Hele-Shaw cells have been performed by Maxworthy [45]. Nevertheless, and unfortunately, only a brief description of initial experimental results is presented in Ref. [45]: essentially, it has been found that the net effect of the small gap gradient in a diverging cell is to destabilize the interface. This is in line with the analytical linear stability results obtained in Ref. [43]. Regrettably, to the best of our knowledge, a more comprehensive account of Maxworthy's experiments in diverging radially tapered Hele-Shaw cells has never been published. Only very recently, Bongrand and Tsai [46] have performed experiments in converging radially tapered Hele-Shaw cells, and presented results demonstrating the stabilization effects of a negative gap gradient. Also recently, Pihler-Puzović *et al.* [47,48] studied experimentally the radial displacement of a viscous oil by a gas injected in an elastic-walled Hele-Shaw cell, where the rigid upper cell plate has been replaced by a flexible membrane. It has been found that the

elastic membrane provides a radially tapered converging flow passage that can indeed stabilize radial viscous fingering.

On the theoretical side, a recent investigation performed by Jackson *et al.* [44] analyzed fully nonlinear, late-time stages of the flow in radially tapered Hele-Shaw cells through sophisticated numerical simulations. As opposed to previous studies [40,43], instead of targeting the control of the fingering instabilities, Ref. [44] focuses on a different but also appealing aspect of fluid displacements in small gap gradient radial Hele-Shaw cells. Motivated by the dissimilar interfacial behaviors at low and high capillary numbers in tapered *rectangular* Hele-Shaw cells [38–40] (e.g., in converging cells finger tips are smooth and wide at low Ca, and sharp at high Ca), they investigated the possibility of a viscous fingering instability transition in tapered *radial* Hele-Shaw geometry. Therefore, rather than aim attention at a specific capillary number regime (either low or high, as done in the rectangular cell cases studied in Refs. [38–40]), the authors in Ref. [44] used their powerful numerical techniques to systematically scrutinize the transition in fingering behavior in radial tapered cells by varying the capillary number at fully nonlinear time stages of the flow. Their central results can be summarized as follows: in converging (diverging) radial cells the effects change from stabilizing (destabilizing) at low Ca, to destabilizing (stabilizing) at high Ca.

As stressed in Ref. [44], in their work (and also in our current paper) the stabilizing or destabilizing concepts refer to the behavior of the radially tapered situations as compared with the corresponding interface response in the parallel-plate (or, uniform) radial Hele-Shaw cell case. For example, in the low-Ca regime mentioned above, when one says that the tapered interface is stabilized, what one really means is that the tapered situation is stabilized with respect to the equivalent situation observed in the uniform cell case. Nevertheless, such a tapered-cell relatively stabilized interface can still be unstable, in the sense that it can still be deformed (i.e., noncircular), and present sizable fingering structures. So, in the end, we deal with the concept of a "relative stability" (or, equivalently a "relative instability") in which a tapered interface is always compared with a corresponding interface that emerges in a uniform Hele-Shaw cell.

Regarding the relative changes in the morphology and size of the resulting fingering structures, it has been found [44] that for a fixed gap-gradient value, the width of the fingers tend to get wider, and flatten at their tips as Ca is increased, leading to the occurrence of finger-tip-splitting phenomena at larger values of Ca. These fully nonlinear interface responses to changes in Ca are clearly illustrated in Fig. 6 of Ref. [44]. Moreover, if Ca is kept fixed, and the sign of the gap gradient is reversed, one can observe fingering patterns of different sizes. It has been verified that linear stability analysis does not accurately predict the point (i.e., the critical value of the capillary number) at which the relative stability transitions. This critical capillary number ($\mathrm{Ca}_{\mathrm{crit}}$) indicates the situation at which a relatively stable interface becomes relatively unstable, in comparison to the equivalent interface in a uniform cell. It has also been shown that the linear stability theory prediction for $\mathrm{Ca}_{\mathrm{crit}}$ overestimates its magnitude in comparison to the more robust prediction based on their fully nonlinear simulations. This discrepancy has been attributed to the neglect by the linear stability calculation of the important nonlinear effects naturally incorporated by late-time numerical computations.

From what we have discussed in the previous paragraphs, it is clear that the studies carried out so far on viscous fingering pattern formation in radially tapered Hele-Shaw cells mainly focus either on the analytical linear stability analysis [43] of the problem, or rely heavily on laborious numerical simulations [44]. These analytical and numerical investigations provide a good understanding of the pattern-formation process in the initial (purely linear), and final (fully nonlinear) time regime. Nonetheless, a study of the dynamics that bridges these two extremes in tapered radial Hele-Shaw cells is still lacking. Our main purpose in this work is to carry out the weakly nonlinear analysis for the intermediate stages of interface evolution in radially tapered cells, focusing on the onset of nonlinear effects. We concentrate our attention on trying to get useful insights into the most important ingredients of the fingering instability transition numerically studied in Ref. [44], at just the lowest nonlinear order, and through predominantly analytical means. Our aim is to use the simplest extension of perturbation theory beyond linear stability (i.e., a second-order mode-coupling

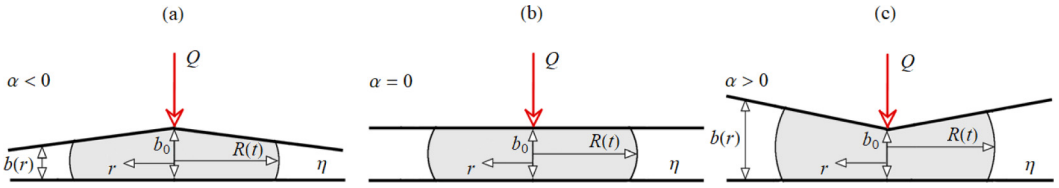

FIG. 1. Illustrative sketch of the side view of the injection-driven fluid displacements in three kinds of radial Hele-Shaw cells: (a) converging ($\alpha < 0$), (b) uniform ($\alpha = 0$), and (c) diverging ($\alpha > 0$), where $\alpha = db(r)/dr$ denotes the small gap gradient, $b(r)$ is the variable gap thickness, r is the radial coordinate, and $b_0 = b(r = 0)$. The time-dependent unperturbed interface radius is represented by $R(t)$. Moreover, Q denotes the volumetric injection flow rate, η is the outer (displaced) fluid viscosity, while the inner (displacing) fluid (in gray) has negligible viscosity.

theory) and still be able to extract valuable information about some of the most relevant nonlinear aspects of the problem.

The remainder of this paper is organized as follows. Section II presents a derivation of a mode-coupling equation that describes the time evolution of the interfacial perturbation amplitudes for the radially tapered Hele-Shaw cell problem. In Sec. III we discuss the influence of the capillary number on the relative instability transition at early nonlinear stages of the flow. We concentrate our attention on trying to comprehend how the length and overall shape of the fingers (special attention is given to the emblematic tip-splitting events) are impacted by Ca, and by the sign of the small gap gradient. Our final conclusions are compiled in Sec. IV.

II. MODE-COUPLING DIFFERENTIAL EQUATION FOR THE PERTURBATION AMPLITUDES

In this work, we follow previous studies in tapered Hele-Shaw flows [38–40], and consider a situation which has also been largely explored both theoretically and experimentally in parallel-plate, radial, and rectangular Hele-Shaw cells [1,4,6–11]. We focus on the limit of infinite viscosity ratio $\beta = \eta_{\text{outer}}/\eta_{\text{inner}}$, where the viscosity of the inner fluid is negligible compared with the viscosity η of the outer fluid. The limit of infinite viscosity ratio is expected to agree well with situations in which a very viscous oil is displaced by a gas, where $10^4 \leqslant \beta \leqslant 10^5$ [4,46–48]. Note that this is not exactly similar to the situations studied numerically in Ref. [44] that considered two-phase flows in small gap gradient radial Hele-Shaw cells under low ($\beta = 10$) and high ($\beta = 1250$), but finite, viscosity ratios.

Consider the geometry of a radially tapered Hele-Shaw cell in which an outer fluid of viscosity η is displaced by the radial injection of an inner fluid with negligible viscosity. The fluids are immiscible and incompressible, and there exists a nonzero surface tension σ between them. The inner fluid is injected at a constant volumetric injection rate Q through an inlet located at the center of the upper cell plate. In contrast to the conventional parallel-plate setup, the upper plate has a constant small depth gradient α ($|\alpha| \ll 1$) in the radial direction. Depending on the sign of α, we can have three types of radial Hele-Shaw cells (see Fig. 1): (a) converging ($\alpha < 0$), (b) uniform ($\alpha = 0$), and (c) diverging ($\alpha > 0$). The coordinate system is defined in such a way that its origin is located at the center of the cell, and r denotes the radial coordinate. In this framing, the cell gap varies linearly with the radial distance r such that it can be written as $b(r) = b_0 + \alpha r$, where $b_0 = b(r = 0)$ is the cell spacing at its center.

During the injection process, the initially unperturbed, circular interface can become unstable, and deform, due to the interplay of viscous and capillary forces. Therefore, we express the perturbed interface as $\mathcal{R} = \mathcal{R}(\theta, t) = R(t) + \zeta(\theta, t)$, where $R = R(t)$ is the time-dependent unperturbed radius of the interface, and θ denotes the azimuthal angle in the $r - \theta$ plane. The net interface

disturbance is represented as a Fourier series,

$$\zeta(\theta,t)=\sum_{n=-\infty}^{+\infty}\zeta_n(t)\exp(in\theta), \tag{1}$$

where $\zeta_n(t)$ denotes the complex Fourier amplitudes, with integer wave numbers n, and $|\zeta|\ll R$. Note that for $\mathcal{R}$ to be real, the complex conjugate function ζ_n^* must satisfy the condition $\zeta_n^*=\zeta_{-n}$. The inclusion of the mode $n=0$ is done to keep the volume of the perturbed shape independent of the perturbation ζ in radially tapered cells. In this way, we conveniently rewrite the variable cell gap in terms of $R(t)$ as

$$b(r,t)=b_i(t)+\alpha[r-R(t)], \tag{2}$$

where the cell spacing at $r=R(t)$ is given by

$$b_i=b_i(t)=b_0+\alpha R(t). \tag{3}$$

Since we are interested in the small depth gradient $|\alpha|\ll 1$ limit, we consider that

$$\frac{|\alpha|R}{b_i}\ll 1, \tag{4}$$

which implies that $|\alpha(r-R)|=|\alpha\zeta|\ll b_i$. It should be emphasized that throughout this work our perturbative weakly nonlinear approach keeps terms up to second order in ζ, and up to first order in the rescaled slope $\alpha R/b_i$.

Conservation of volume

$$Qt+\pi b_0R_0^2+\frac{2\alpha}{3}\pi R_0^3=\int_0^{2\pi}\left(\frac{b_0\mathcal{R}^2}{2}+\frac{\alpha\mathcal{R}^3}{3}\right)d\theta \tag{5}$$

imposes that up to second order in ζ the zeroth mode is written in terms of the other modes as

$$\zeta_0=-\frac{1}{2R}\left[1+\frac{\alpha R}{b_i}\right]\sum_{n=1}^{\infty}[|\zeta_n(t)|^2+|\zeta_{-n}(t)|^2]. \tag{6}$$

By using Eq. (5) and considering the situation in which the fluid-fluid interface is unperturbed [$\mathcal{R}=R(t)$], one obtains an useful relation that expresses as $R(t)$ evolves in time

$$\pi b_0\left[R^2(t)-R_0^2\right]+\frac{2\alpha}{3}\pi\left[R^3(t)-R_0^3\right]=Qt, \tag{7}$$

where $R_0=R(t=0)$ is the unperturbed interface radius at $t=0$. Notice that by taking the time derivative of Eq. (7) one obtains that $Q=2\pi R\dot{R}b_i$, where $dR/dt=\dot{R}$.

The basic hydrodynamic equation of the problem is Darcy's law [4]

$$\mathbf{v}=-\frac{b^2(r,t)}{12\eta}\boldsymbol{\nabla}P, \tag{8}$$

where $\mathbf{v}=\mathbf{v}(r,\theta)$, $P=P(r,\theta)$ are the gap-averaged velocity, and pressure, respectively. The incompressibility condition for the smoothly varying gap situation is given by [38,39,49]

$$\boldsymbol{\nabla}\cdot[b(r,t)\mathbf{v}]=0. \tag{9}$$

Substituting Eq. (8) into Eq. (9), and using Eq. (4), we obtain a partial differential equation for the pressure

$$\nabla^2P+\frac{3\alpha}{b_i}\frac{\partial P}{\partial r}=0. \tag{10}$$

The most general solution of Eq. (10) can be written as [39,49]

$$P(r,\theta) = f(r) + \sum_{n\neq 0} g_n(r) e^{in\theta}. \tag{11}$$

Substituting Eq. (11) into Eq. (10), we have

$$\frac{1}{r}\frac{d}{dr}\left(r\frac{df}{dr}\right) + \frac{3\alpha}{b_i}\frac{df}{dr} = 0 \tag{12}$$

and

$$\frac{1}{r}\frac{d}{dr}\left(r\frac{dg_n}{dr}\right) + \frac{3\alpha}{b_i}\frac{dg_n}{dr} - \frac{n^2}{r^2}g_n = 0. \tag{13}$$

Note that Eq. (11) separates two different contributions in the pressure field: $f(r)$ which comes from a propagating circular interface, and $g_n(r)$ that is due to the harmonic disturbance of the interface. In this context, df/dr is the pressure gradient for an unperturbed interface growing with velocity $v_r = \dot{R}$, that satisfies Darcy's law (8)

$$\left.\frac{df}{dr}\right|_{r=R} = -\frac{12\eta\dot{R}}{b_i^2}. \tag{14}$$

In order to solve Eq. (12), we define a new variable $\psi(r) \equiv rf'(r)$. Then we rewrite Eq. (12) in terms of ψ, and integrate to obtain

$$\frac{df}{dr} = \frac{\psi(R)}{r}\exp\left[-\frac{3\alpha}{b_i}(r-R)\right], \tag{15}$$

where $\psi(R)$ can be determined using the condition (14). Integrating Eq. (15), the solution for $f(r)$ can be written as

$$f(r) = \psi(R)\int \frac{1}{r}\exp\left[-\frac{3\alpha}{b_i}(r-R)\right]dr + C, \tag{16}$$

where C is a constant of integration.

On the other hand, by applying the Frobenius method [50] to solve Eq. (13), and using the condition $\lim_{r\to\infty} g_n(r) = 0$ for the situation in which $\alpha = 0$, we have (for $n \neq 0$)

$$g_n(r) = \sum_{k=0}^{\infty} P_k^{(n)}\left(\frac{r}{R}\right)^{k-|n|}, \tag{17}$$

where the coefficients $P_k^{(n)}$ are related to one another by the recurrence relation (for $k > 0$)

$$P_k^{(n)} = -\frac{3\alpha}{b_i}\left[\frac{(k-|n|-1)}{k(k-2|n|)}\right]P_{k-1}^{(n)}. \tag{18}$$

Finally, by using the solutions (16) and (17), as well as the recurrence relation (18), the pressure [Eq. (11)] can be written as

$$\begin{aligned} P(r,\theta) = {} & \psi(R)\int \frac{1}{r}\exp\left[-\frac{3\alpha}{b_i}(r-R)\right]dr \\ & + \sum_{n\neq 0} P^{(n)}(t)\left\{\left(\frac{r}{R}\right)^{-|n|} + \frac{3\alpha R}{b_i}\left[\frac{|n|}{1-2|n|}\right]\left(\frac{r}{R}\right)^{1-|n|}\right\}\exp(in\theta) + C. \end{aligned} \tag{19}$$

As we assume the rescaled slope $|\alpha|R/b_i \ll 1$ [Eq. (4)] in the solution of $g_n(r)$, we keep terms up to first order in $\alpha R/b_i$.

At this point, we have all the elements needed to perform a weakly nonlinear analysis of the system. To find a relation between $P^{(n)}(t)$ in Eq. (19) and the perturbation amplitudes $\zeta_n(t)$ in Eq. (1), we consider the kinematic boundary condition which states that the normal components of fluid velocity at the interface equals the velocity of the interface itself [4]

$$\frac{\partial \mathcal{R}}{\partial t} = \left(v_r - \frac{1}{r}\frac{\partial \zeta}{\partial \theta} v_\theta \right)\Big|_{r=\mathcal{R}}, \tag{20}$$

where v_r and v_θ are the radial and azimuthal components of the depth-averaged velocity $\mathbf{v}$, respectively. We keep terms up to second order in ζ, and then Fourier transform. Solving for $P^{(n)}(t)$ consistently yields

$$\begin{aligned} P^{(n)}(t) = {} & \frac{\dot{\zeta}_n}{K(n)} + \frac{1}{K(n)}\frac{\dot{R}}{R}\left[1 + \frac{\alpha R}{b_i}\right]\zeta_n - \frac{1}{K(n)}\frac{\dot{R}}{R^2}\left[1 + \frac{\alpha R}{b_i}\right]\sum_{n'\neq 0}\zeta_{n'}\zeta_{n-n'} \\ & + \frac{b_i^2}{12\eta}\frac{\dot{R}}{R}\sum_{n'\neq 0}\frac{1}{K(n)K(n')}\left\{M(n,n') + \frac{3\alpha R}{b_i}\left[N(n,n') - \frac{2|n'|}{3R^2} + \frac{1}{3}M(n,n')\right]\right\}\zeta_{n'}\zeta_{n-n'} \\ & + \frac{b_i^2}{12\eta}\sum_{n'\neq 0}\frac{1}{K(n)K(n')}\left\{M(n,n') + \frac{3\alpha R}{b_i}\left[N(n,n') - \frac{2|n'|}{3R^2}\right]\right\}\dot{\zeta}_{n'}\zeta_{n-n'}. \end{aligned} \tag{21}$$

Here the functions $K(n)$, $M(n,n')$, and $N(n,n')$ stand for

$$K(n) = \frac{b_i^2}{12\eta R}\left[|n| - \frac{3\alpha R}{b_i}\frac{|n|(1-|n|)}{1-2|n|}\right], \tag{22}$$

$$M(n,n') = \frac{n'(n-n') + |n'|(|n'|+1)}{R^2}, \tag{23}$$

and

$$N(n,n') = \frac{n'|n'|(n-n') - n'^2(1-|n'|)}{(1-2|n'|)R^2}. \tag{24}$$

The other important boundary condition is the pressure jump at the interface, which is given by the Young-Laplace equation [1,4]

$$P(r=\mathcal{R},\theta) = -\left[\frac{\pi}{4}\sigma\kappa + \frac{2\sigma\cos\phi}{b(r,t)}\right]\Big|_{r=\mathcal{R}}. \tag{25}$$

In Eq. (25), κ denotes the interface curvature in the plane of the cell and can be written, up to second order in the perturbation ζ, as

$$\begin{aligned} \kappa &= \frac{\mathcal{R}^2 + 2\left(\frac{\partial \mathcal{R}}{\partial \theta}\right)^2 - \mathcal{R}\frac{\partial^2 \mathcal{R}}{\partial \theta^2}}{\left[\mathcal{R}^2 + \left(\frac{\partial \mathcal{R}}{\partial \theta}\right)^2\right]^{3/2}} \\ &= \frac{1}{R} - \frac{1}{R^2}\left(\zeta + \frac{\partial^2 \zeta}{\partial \theta^2}\right) + \frac{1}{R^3}\left[\zeta^2 + \frac{1}{2}\left(\frac{\partial \zeta}{\partial \theta}\right)^2 + 2\zeta\frac{\partial^2 \zeta}{\partial \theta^2}\right] + O(\zeta^3/R^4). \end{aligned} \tag{26}$$

On the other hand, the term proportional to $1/b(r,t)$ is associated with the curvature for the direction across the gap, and ϕ is the static contact angle measured between the plates and the curved fluid meniscus. As in Refs. [40,43,44], we focus on the $\phi = 0$ situation, when the viscous fluid is perfectly wetting. Note the presence of the factor $\pi/4$ in front of κ in Eq. (25), as it is appropriate for the wetting case $\phi = 0$ [32–34].

To obtain the equation of motion for the perturbation amplitude $\zeta_n(t)$, first we substitute Eq. (21) into Eq. (19) evaluated at the interface. Then, we insert the resulting expression into the Young-Laplace condition (25). Keeping terms up to the second order in ζ and first order in $\alpha R/b_i$, and Fourier transforming, we obtain a dimensionless equation of motion for the perturbation amplitudes (for $n \neq 0$)

$$\dot{\zeta}_n = \left[\lambda(n) + \frac{\alpha R}{b_i}\Lambda(n)\right]\zeta_n + \sum_{n'\neq 0}\left[F(n,n')\zeta^{\rm lin}_{n'}\zeta^{\rm lin}_{n-n'} + G(n,n')\dot{\zeta}^{\rm lin}_{n'}\zeta^{\rm lin}_{n-n'}\right]$$
$$+ \frac{\alpha R}{b_i}\sum_{n'\neq 0}\left[\mathcal{F}(n,n')\zeta^{\rm lin}_{n'}\zeta^{\rm lin}_{n-n'} + \mathcal{G}(n,n')\dot{\zeta}^{\rm lin}_{n'}\zeta^{\rm lin}_{n-n'}\right], \tag{27}$$

where lengths and time are rescaled by R_0, and $R_0^2 b_0/Q$, respectively.

To correctly contemplate the implications of second-order mode coupling, in Eq. (27) we follow Miranda and Widom [11] [see their Eqs. (30)–(32)], and obtain the appropriate segregation between orders in ζ by substituting the purely linear solution of the mode-coupling differential equation

$$\dot{\zeta}^{\rm lin}_n = \left[\lambda(n) + \frac{\alpha R}{b_i}\Lambda(n)\right]\zeta^{\rm lin}_n \tag{28}$$

into the second-order terms appearing on the right-hand side of Eq. (27). The functions associated with the linear growth rate $[\lambda(n) + (\alpha R/b_i)\Lambda(n)]$ are

$$\lambda(n) = \frac{\dot{R}}{R}(|n|-1) - \frac{\pi}{4}\frac{q^2 b_i^2}{{\rm Ca}R^3}|n|(n^2-1) \tag{29}$$

and

$$\Lambda(n) = \frac{\dot{R}}{R}\left(\frac{|n|+1}{2|n|-1}\right) + \frac{2q^2 b_i}{{\rm Ca}R^2}|n| - \frac{\pi}{4}\frac{q^2 b_i^2}{{\rm Ca}R^3}\frac{|n|(n^2-1)}{2|n|-1}, \tag{30}$$

where

$${\rm Ca} = \frac{12\eta Q R_0}{\sigma b_0^3} \tag{31}$$

is the global capillary number [34,44] which expresses a relative measure of viscous to surface tension forces, while $q = R_0/b_0$ is the initial aspect ratio. The global capillary number Ca is an important control parameter of the radially tapered Hele-Shaw cell system and should be distinguished from the local (or instantaneous) capillary number $\overline{\rm Ca} = \eta\dot{R}/\sigma$ which can be orders of magnitude smaller. Typical values of the local capillary number used in tapered Hele-Shaw cell experiments vary within a wide spread range $4.0 \times 10^{-4} \leqslant \overline{\rm Ca} \leqslant 2.5 \times 10^2$ [38,40,46,48].

The mode-coupling terms are given by

$$F(n,n') = \frac{|n|}{R}\left\{\frac{\dot{R}}{R}\left[\frac{1}{2} - {\rm sgn}(nn')\right] - \frac{\pi}{4}\frac{q^2 b_i^2}{{\rm Ca}R^3}\left[1 - \frac{n'}{2}(3n'+n)\right]\right\}, \tag{32}$$

$$G(n,n') = \frac{|n|}{R}\left[1 - {\rm sgn}(nn') - \frac{1}{|n|}\right], \tag{33}$$

$$\mathcal{F}(n,n') = \frac{|n|}{R}\left\{\frac{\dot{R}}{R}\left[\frac{2-|n|}{2|n|-1} + 2{\rm sgn}(nn')\frac{2-|n'|}{2|n'|-1} - \frac{1}{|n|}\right]\right.$$
$$\left. - \frac{\pi}{4}\frac{q^2 b_i^2}{{\rm Ca}R^3}\frac{3}{2|n|-1}\left[1 - \frac{n'}{2}(3n'+n)\right]\right\}, \tag{34}$$

and

$$\mathcal{G}(n,n') = \frac{3|n|}{R}\left[\frac{1}{2|n|-1} + \frac{\mathrm{sgn}(nn')}{2|n'|-1} - \frac{1}{3|n|}\right], \tag{35}$$

where the sgn function equals ± 1 according to the sign of its argument.

While dealing with Eq. (27) one must be careful and avoid possible spurious higher-order dependences on $\alpha R/b_i$. Therefore, in accordance with what has been assumed since the very beginning of our calculation, one must neglect any contributions having higher order than $O(\alpha R/b_i)$. Motivated by this important remark, it is convenient to define a new notation $\zeta_n^{\mathrm{lin}} = \zeta_n^{\mathrm{lin}(0)} + \zeta_n^{\mathrm{lin}(1)}$, where $\zeta_n^{\mathrm{lin}(k)}$ is the correction at kth order in $\alpha R/b_i$ to the linear perturbation amplitude. Consequently, Eq. (28) can be rewritten as

$$\dot{\zeta}_n^{\mathrm{lin}} = \lambda(n)\zeta_n^{\mathrm{lin}} + \frac{\alpha R}{b_i}\Lambda(n)\zeta_n^{\mathrm{lin}(0)}, \tag{36}$$

whose solution can be readily written as

$$\zeta_n^{\mathrm{lin}}(t) = \zeta_n^{\mathrm{lin}(0)}(t) + \zeta_n^{\mathrm{lin}(1)}(t) = \zeta_n^{\mathrm{lin}(0)}(t)\left[1 + \int_0^t \frac{\alpha R}{b_i}\Lambda(n)dt'\right]. \tag{37}$$

Here $\zeta_n^{\mathrm{lin}(0)}(t) = \zeta_n^{\mathrm{lin}(0)}(0)\exp[\int_0^t \lambda(n)dt']$ is the solution of equation $\dot{\zeta}_n^{\mathrm{lin}(0)} = \lambda(n)\zeta_n^{\mathrm{lin}(0)}$. Substituting Eq. (37) into Eq. (27) and neglecting any higher-order contributions than $O(\alpha R/b_i)$, we obtain

$$\begin{aligned}\dot{\zeta}_n = {} & \lambda(n)\zeta_n + \frac{\alpha R}{b_i}\Lambda(n)\zeta_n^{(0)} \\ & + \sum_{n'\neq 0}[F(n,n') + \lambda(n')G(n,n')]\left[\zeta_{n'}^{\mathrm{lin}(0)}\zeta_{n-n'}^{\mathrm{lin}(0)} + \zeta_{n'}^{\mathrm{lin}(0)}\zeta_{n-n'}^{\mathrm{lin}(1)} + \zeta_{n'}^{\mathrm{lin}(1)}\zeta_{n-n'}^{\mathrm{lin}(0)}\right] \\ & + \frac{\alpha R}{b_i}\sum_{n'\neq 0}[\mathcal{F}(n,n') + \lambda(n')\mathcal{G}(n,n') + \Lambda(n')G(n,n')]\zeta_{n'}^{\mathrm{lin}(0)}\zeta_{n-n'}^{\mathrm{lin}(0)},\end{aligned} \tag{38}$$

where $\zeta_n^{(0)}$ is given by

$$\dot{\zeta}_n^{(0)} = \lambda(n)\zeta_n^{(0)} + \sum_{n'\neq 0}[F(n,n') + \lambda(n')G(n,n')]\zeta_{n'}^{\mathrm{lin}(0)}\zeta_{n-n'}^{\mathrm{lin}(0)}. \tag{39}$$

Equation (38) is the mode-coupling equation of the Saffman-Taylor problem for radially tapered Hele-Shaw cells, conveniently written in terms of the three relevant dimensionless parameters of the problem: α, q, and Ca. In fact, Eq. (38) is a central result of this work. After appropriate reintroduction of dimensions, it can be shown that Eq. (38) reduces to the considerably simpler expression obtained in Ref. [11] in the zero-gap-gradient limit ($\alpha = 0$). While the linear growth rate $[\lambda(n) + (\alpha R/b_i)\Lambda(n)]$ composed by Eqs. (29) and (30) provides information about the linear stability of the interface, the nonlinear terms given by Eqs. (32)–(35) offer key insights into the relative instability transition, as well as into the basic morphology of the emerging patterns in the weakly nonlinear regime. We point out that the values we take for our dimensionless parameters throughout this work are consistent with typical physical quantities used in previous experimental, analytical, and numerical investigations in tapered Hele-Shaw cells [38–40,43,44,46–48].

III. FINGERING INSTABILITY TRANSITION IN THE WEAKLY NONLINEAR REGIME

To examine the role played by the capillary number Ca on the viscous fingering instability transition in radially tapered Hele-Shaw cells, we need to describe the time evolution of the perturbed interface $\mathcal{R}$ for converging ($\alpha < 0$) and diverging ($\alpha > 0$) cells, and then compare the resulting interface shapes with the corresponding interface obtained in a uniform cell ($\alpha = 0$). Furthermore, we want to do this by capturing important weakly nonlinear effects, via a perturbative

mode-coupling scheme that keeps terms up to second order in ζ and up to first order in $\alpha R/b_i$. This approach is able to bring to light some fundamental aspects of the relative stability behavior and of the morphology of the resulting interfacial patterns. In this context, it is essential to figure out how Ca influences the shape of the emerging fingers, in particular with respect to the development of the finger-tip-widening, -splitting, and -sharpening phenomena.

Within the scope of our mode-coupling theory, it has been shown that finger-tip widening, splitting, and sharpening are behaviors related to the influence of a fundamental mode n on the growth of its harmonic mode $2n$ [11]. In other words, it has been demonstrated that these basic pattern-forming phenomena can be predicted, captured and properly described already at second order in the perturbation amplitudes, and by considering the nonlinear coupling between just two Fourier modes, namely, n and $2n$. Therefore, to tackle finger-tip morphology and relative stability issues at the weakly nonlinear level in radially tapered geometry, it is convenient to rewrite the net interface perturbation $\zeta(\theta, t)$ [Eq. (1)] in terms of these two specific Fourier modes

$$\zeta(\theta, t) = \zeta_0(t) + a_n(t)\cos(n\theta) + a_{2n}(t)\cos(2n\theta), \tag{40}$$

where for a given mode $a_n(t) = [\zeta_n(t) + \zeta_{-n}(t)]$ denotes the real-valued cosine amplitudes. Without loss of generality, as in Ref. [11] we choose the phase of the fundamental mode so that $a_n > 0$. Notice that the term ζ_0 in Eq. (40) expresses an intrinsically nonlinear concern [i.e., it consists of a second-order correction in ζ, as shown in Eq. (6)], so that in the purely linear regime one can simply set $\zeta_0 = 0$. We direct the interested readers to Refs. [8,11,51–54] for a detailed discussion about the mode-coupling strategy, its description and proposed interpretation of the typical pattern-forming mechanisms occurring in both rectangular and radial Hele-Shaw flows.

It is apparent from Eq. (40) that to describe the time evolution of the perturbed interface $\mathcal{R}(\theta, t)$, one needs to know how the cosine amplitudes $a_n(t)$ and $a_{2n}(t)$ evolve in time. To do that, we rewrite the mode-coupling equation (38) in terms of cosine modes, considering the interplay of modes n and $2n$, to obtain the following forced linear differential equations:

$$\begin{aligned}
\dot{a}_n = {} & \lambda(n)a_n + \frac{\alpha R}{b_i}\Lambda(n)a_n^{(0)} + \frac{1}{2}\Bigg\{[F(n,-n) + F(n,2n) + \lambda(n)G(n,-n) + \lambda(2n)G(n,2n)] \\
& \times \left[a_n^{\mathrm{lin}(0)}a_{2n}^{\mathrm{lin}(0)} + a_n^{\mathrm{lin}(0)}a_{2n}^{\mathrm{lin}(1)} + a_n^{\mathrm{lin}(1)}a_{2n}^{\mathrm{lin}(0)}\right] \\
& + \frac{\alpha R}{b_i}[\mathcal{F}(n,-n) + \mathcal{F}(n,2n) + \lambda(n)\mathcal{G}(n,-n) + \lambda(2n)\mathcal{G}(n,2n) \\
& + \Lambda(n)G(n,-n) + \Lambda(2n)G(n,2n)]a_n^{\mathrm{lin}(0)}a_{2n}^{\mathrm{lin}(0)}\Bigg\},
\end{aligned} \tag{41}$$

$$\begin{aligned}
\dot{a}_{2n} = {} & \lambda(2n)a_{2n} + \frac{\alpha R}{b_i}\Lambda(2n)a_{2n}^{(0)} + \frac{1}{2}\Bigg\{[F(2n,n) + \lambda(n)G(2n,n)] \\
& \times \left[a_n^{\mathrm{lin}(0)}a_n^{\mathrm{lin}(0)} + a_n^{\mathrm{lin}(0)}a_n^{\mathrm{lin}(1)} + a_n^{\mathrm{lin}(1)}a_n^{\mathrm{lin}(0)}\right] \\
& + \frac{\alpha R}{b_i}[\mathcal{F}(2n,n) + \lambda(n)\mathcal{G}(2n,n) + \Lambda(n)G(2n,n)]a_n^{\mathrm{lin}(0)}a_n^{\mathrm{lin}(0)}\Bigg\}.
\end{aligned} \tag{42}$$

The analytical solution for this type of differential equation has been examined in Ref. [11] [see their Eq. (28), plus their Eqs. (30)–(32)]. Of course, the time evolution of the amplitudes $a_n(t)$ and $a_{2n}(t)$ can also be readily obtained by numerically solving Eqs. (41)–(42).

To characterize the overall shape of the patterns at the onset of nonlinear effects for each value of the gap gradient ($\alpha < 0$, $\alpha = 0$, and $\alpha > 0$) and also to quantify their relative instability behavior, we use a quantity defined by the inner and outer radial envelopes of the pattern as (see Fig. 2)

$$\Delta\mathcal{R} = \mathcal{R}_{\max} - \mathcal{R}_{\min}. \tag{43}$$

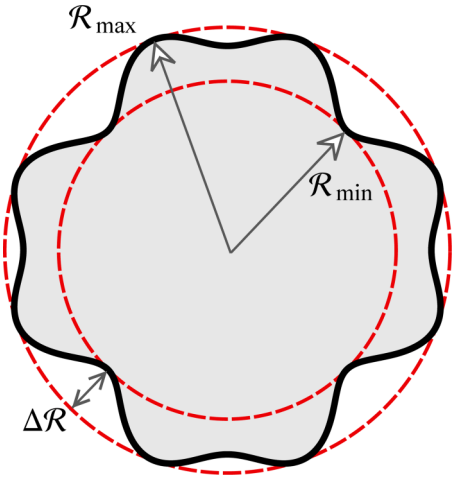

FIG. 2. Characteristic lengths defining the finger length function $\Delta\mathcal{R}$ as defined in Eq. (43): $\mathcal{R}_{\max}$ is the maximum value of the radial coordinate of the deformed interface (located at a finger tip), and $\mathcal{R}_{\min}$ is the corresponding minimum radius (located at a finger valley).

The quantity $\Delta\mathcal{R}$ can be viewed as a typical finger length scale which describes the finger perturbation amplitude in terms of two lengths: (1) the maximum value of the perturbed interface radius ($\mathcal{R}_{\max}$) which in Fig. 2 is illustrated by the dashed outer circle that encloses the entire pattern, being tangent to the finger tips, and (2) the minimum value of the perturbed interface radius ($\mathcal{R}_{\min}$) depicted by the dashed inner circle in Fig. 2 which is tangential to the finger valleys. Bischofberger *et al.* [12] adopted a similar approach to successfully quantify the large-scale structure, emergent global features, and the nonlinear growth of fingering patterns in uniform (parallel-plate) radial Hele-Shaw cells. Equations (40)–(43) will be utilized to gain insight into the relative instability transition in radially tapered Hele-Shaw geometry. Note that one can calculate the quantity $\Delta\mathcal{R}$ analytically by considering the interaction of modes n and $2n$ as expressed in Eq. (40). By evaluating $\partial\mathcal{R}/\partial\theta = 0$, we find the positions for the maximum and minimum values of the perturbed interface radius $\mathcal{R}$, yielding

$$\cos(n\theta) = \pm 1 \tag{44}$$

and

$$\cos(n\theta) = -\frac{a_n}{4a_{2n}}. \tag{45}$$

For the situation in which $|a_n| > 4|a_{2n}|$, the fingers do not split at their tips, and we have only Eq. (44) to express possible solutions, implying that $\Delta\mathcal{R} = 2a_n$. Nonetheless, if $|a_n| < 4|a_{2n}|$ the fingers tend to split at their tips (as in the situation illustrated in Fig. 2), and we have also to consider Eq. (45) as a valid solution. In this case, $\Delta\mathcal{R} = a_n - a_n^2/8a_{2n} - 2a_{2n}$.

Before we proceed to our weakly nonlinear analysis of the radially tapered Hele-Shaw cell system, we make some necessary remarks on the results that will be presented in the remainder of this work. First, one should realize that our perturbative weakly nonlinear approach holds at the onset of nonlinearities, where the interfacial disturbances ζ are considerably smaller than the corresponding unperturbed interface radius R. Additionally, for the sake of simplicity and to better understand the mechanisms behind the pattern-formation process, our weakly nonlinear description considers the coupling of a small number of relevant Fourier modes [8,11]. Consequently, the readers should not expect that our weakly nonlinear interfacial patterns, and other related predictions will quantitatively reproduce the fully nonlinear features obtained in the intensive numerical simulations of the radially

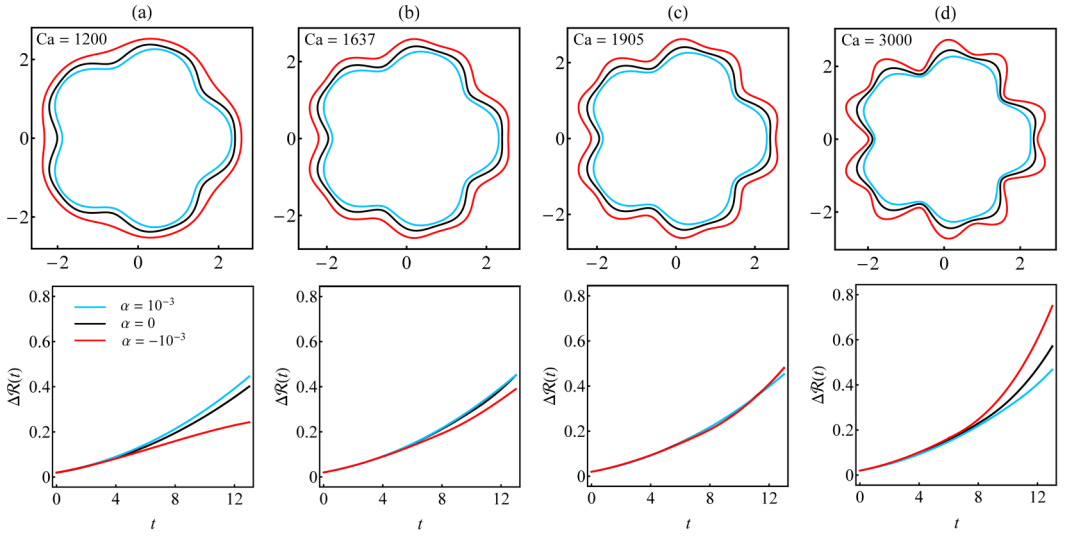

FIG. 3. Snapshot of the weakly nonlinear interfaces at time $t = t_f = 13$ (top panels), illustrating typical fingering patterns for injection-driven radial flow in diverging ($\alpha = 10^{-3}$), uniform ($\alpha = 0$), and converging ($\alpha = -10^{-3}$) Hele-Shaw cells. The following values of the capillary number are analyzed: (a) Ca = 1200, (b) Ca = 1637, (c) Ca = 1905, and (d) Ca = 3000. The interfaces are obtained by considering the nonlinear coupling between modes n and $2n$, where $n = 5$. The corresponding time evolution of the finger length $\Delta\mathcal{R}(t)$ for $0 \leqslant t \leqslant t_f$ is shown in the bottom panels.

tapered Hele-Shaw cell problem performed in Ref. [44]. Their simulations focus on the late-time nonlinear stages of pattern evolution, where the finger sizes are large and the finger shapes are generally more complex than the ones we present in our current study. So, we have no intention to exactly recreate the specific late-time results obtained in Ref. [44]. Instead, we seek to extract as much information as possible about some of the most fundamental features of the instability transition in tapered cells by employing a relatively simple theoretical tool.

Regardless of the limitations discussed above, our mode-coupling model still provides valuable information about the role of nonlinear effects at early stages of the dynamics. Most importantly, it furnishes key indications about the morphology of the fingering structures (e.g., finger broadening, finger narrowing, and finger-tip splitting). It is worthwhile to note that this is something that cannot be accomplished by purely linear stability analysis. At the linear level, the Fourier modes decouple, and the basic mode-coupling ingredients responsible for providing a reliable mimic of the interface shape are completely absent. Therefore, while linear stability analysis does offer access to the linear *absolute* stability of the interface by essentially taking into consideration the action of a single mode, our weakly nonlinear scheme gives useful clues about the ultimate shape of the emerging patterns. This is done already at lowest nonlinear (second-order) level, and considering the coupling of the minimum possible number of interacting Fourier modes (just two). The accessibility to more details about the actual interface shape via the weakly nonlinear formulation will be instrumental to provide guidance for determining the particular value of the capillary number ($\mathrm{Ca}_{\mathrm{crit}}$) at which the *relative* stability makes a transition in small gap gradient radial Hele-Shaw flows.

We begin our discussion by analyzing Fig. 3, which investigates relative instability issues in radially tapered cells when the capillary number is increased: (a) 1200, (b) 1637, (c) 1905, and (d) 3000. The choice of these specific values of Ca will be better understood during our discussion of Fig. 3. In the top panels of Fig. 3, for each value of Ca, we depict the resulting weakly nonlinear interfaces for three representative values of the gap gradient, namely $\alpha = 10^{-3}$ (diverging cell), $\alpha = 0$ (uniform cell), and $\alpha = -10^{-3}$ (converging cell), at a time $t = t_f = 13$. The determination of the final time t_f at which all interfaces are plotted will be discussed below. It should be noted

that the values of α we use throughout this work ($-10^3 \leqslant \alpha \leqslant 10^3$) are precisely the typical values utilized in existing experimental and theoretical studies in tapered Hele-Shaw cells [38–46]. In addition, as in Ref. [44], during the course of our investigation we consider a characteristic initial aspect ratio for the system given by $q = 100$. Moreover, recall that all through this study we focus on the infinite viscosity ratio limit $\beta \to \infty$.

The interfacial patterns displayed in Fig. 3 and in other figures in this paper consider the interaction of two cosine modes n, and $2n$, where in Fig. 3 we take $n = 5$. The choice of $n = 5$ in Fig. 3 as the fundamental mode is made without loss of generality: it turns out that $n = 5$ is an unstable mode at $t = 0$ [$\dot{\zeta}_5(0) > 0$]. If one chooses other unstable Fourier mode as being the fundamental mode at $t = 0$, the basic physical results are similar to the ones obtained for $n = 5$ (another value of n will be examined in Fig. 6). In the bottom panels of Fig. 3, we plot the corresponding time evolution of the finger length $\Delta\mathcal{R}$ [Eq. (43)] for the same three values of α considered in the top panels. All patterns shown in Fig. 3 have the same initial amplitudes, $a_n(0) = 10^{-2}$ and $a_{2n}(0) = 0$.

Throughout this work, the initial amplitude of the first harmonic mode $2n$ is set to zero to ensure that the *initial* growth of this mode is driven solely by *nonlinear* effects. However, by inspecting Eq. (42) one observes that for *subsequent* times a_{2n} is nonzero, and the linear terms start to act. As time advances, the growth of mode $2n$ is essentially determined by a dominant *linear* contribution, assisted by a relatively smaller nonlinear term proportional to a_n^2, forcing the growth of $a_{2n} < 0$. So, within the scope of our weakly nonlinear approach, when the magnitude of a_{2n} increases further, its growth is mostly due to the effect of the linear terms in the equation of motion (42), but properly adjusted by a smaller nonlinear contribution. Nevertheless, the contribution of the first harmonic will induce important changes in the shape of the evolving fingers [11]. The important point here is that the weakly nonlinear coupling dictates the sign of the harmonic mode, whose amplitude goes negative although its initial value was zero. With this particular phase of mode $2n$ forced by the dynamics, the n fingers of the fundamental mode n tend, first to spread, and later, to split. Similar behavior for the fundamental and harmonic modes was found in numerical studies of solidification [55]. Of course, due to the initial condition $a_{2n}(0) = 0$, the harmonic mode $2n$ would not grow if the dynamics were solely restricted to purely linear contributions, and finger widening and splitting would not occur. In this case, only purely sinusoidal shaped fingers would emerge. By applying the initial conditions $a_n(0) = 10^{-2}$ and $a_{2n}(0) = 0$ we guarantee that the phenomena of finger widening and splitting are spontaneously induced by the weakly nonlinear terms in Eqs. (41) and (42). Notice that, different sets of parameters, involving other values of n, $a_n(0)$, t_f, and Ca will also be explored and discussed in this section.

Before we advance, we take a moment to explain how we determine the final time t_f. The interfaces shown in Fig. 3 for various Ca and α have been obtained after time has evolved in the interval $0 \leqslant t \leqslant t_f$. It should be stressed that the values of the final time t_f used in Fig. 3, and in other parts of this work are not arbitrary. To determine t_f, we follow an approach originally proposed by Gingras and Rácz [56] for the linear regime, and extend its range of applicability to the weakly nonlinear stage of evolution. While plotting the interfaces depicted in this paper, we stop the time evolution of the patterns as soon as the base of the fingers starts to move inwards, which would make successive interfaces cross one another. This criterion for determining t_f is justified by the fact that the crossing of successive time evolving interfaces (i.e., the occurrence of backward interface motion) is detected neither in experiments [4,9,10] nor in numerical simulations [57–61] of radial Hele-Shaw flows in which $\beta \to \infty$. Therefore, we adopt $t = t_f$ as the upper bound time for the validity of our perturbative approach. In this framework, and within the scope of our mode-coupling theory, t_f is set by the condition

$$\left[\frac{d\mathcal{R}}{dt}\right]_{t=t_f} = [\dot{R}(t) + \dot{\zeta}(\theta, t)]_{t=t_f} = 0, \tag{46}$$

where Eq. (46) is evaluated by using our weakly nonlinear mode-coupling equation (38).

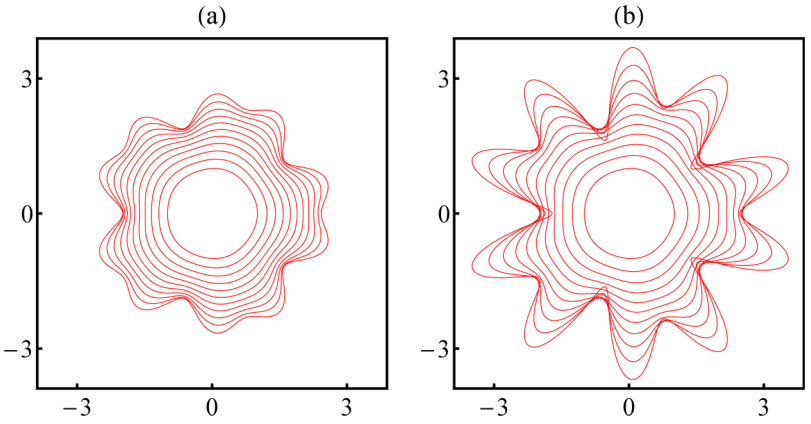

FIG. 4. Snapshots of the evolving interface for the most unstable situation examined in Fig. 3 [i.e., the case for Ca = 3000, and $\alpha = -10^{-3}$ illustrated in Fig. 3(d)], plotted at equal time intervals ($\Delta t = 1$) when (a) $0 \leqslant t \leqslant t_f$, and (b) $0 \leqslant t \leqslant t_f + 5$, where $t_f = 13$. Interface self-intersections are evident in panel (b). Since these self-intersections are not observed in radial Hele-Shaw cell systems in which $\beta \to \infty$, we use $t = t_f$ as the upper bound time for the validity of our weakly nonlinear perturbative approach.

When several values of Ca and α are considered (e.g, as in Fig. 3), we take the final time t_f associated with the most unstable situation (i.e., the case of largest Ca, and for the $\alpha < 0$ of largest magnitude). For example, in Fig. 3 the final time t_f has been determined by considering the situation in which Ca = 3000 and $\alpha = -10^{-3}$ [Fig. 3(d)]. Of course, if interface self-intersections are avoided in the most unstable case, they will not occur in the other (less unstable) situations analyzed in Fig. 3. The importance of properly determining t_f is clearly illustrated Fig. 4: Fig. 4(a) depicts the time evolution for $0 \leqslant t \leqslant t_f$ where $t_f = 13$, that leads to the most unstable interface displayed in Fig. 3(d). On the other hand, Fig. 4(b) shows the same interface evolution, but now up to a time $t = t_f + 5 = 18$. Notice that some interfaces do cross one another Fig. 4(b) indicating that for such a large time our perturbative approach is no longer properly describing the interface evolution. Once again, we point out that the weakly nonlinear analysis does not necessarily remain quantitatively accurate all the way to $t = t_f$. After all, in this work and in Ref. [56] it is argued only that the analysis cannot be valid past t_f, and not rigorously shown that it must be valid for all $t \leqslant t_f$. Consequently, it should be clear that, rigorously speaking, our predictions for $\mathrm{Ca}_{\mathrm{crit}}$, and for the time at which finger-tip-splitting events occur can *a priori* only be expected to be approximations. A more precise account of the quantitative accuracy of the weakly nonlinear expansion for the radially tapered Hele-Shaw flows could be checked by fully nonlinear simulations, like the ones employed in Ref. [44].

After presenting the relevant parameters of the system, and after clarifying the way we determine the final time t_f, now we turn to the discussion of Fig. 3. By examining the top panel in Fig. 3(a), one immediately verifies that for such a capillary number value (Ca = 1200), the converging interface ($\alpha = -10^{-3}$) is not very much distorted from a perfectly circular shape, in the sense that just modestly deformed fingers having small perturbation amplitudes are formed. It is also clear that the converging interface is less deformed than the uniform interface ($\alpha = 0$). This indicates that the converging geometry has a stabilizing effect relative to the equivalent behavior observed under parallel-plate circumstances. On the other hand, the diverging case interface ($\alpha = 10^{-3}$) looks similar to the parallel-plate one, perhaps being just a bit more deformed. Moreover, no finger-tip-splitting events are observed. These findings are qualitatively consistent with the numerical results of Ref. [44] for lower values of Ca, where no finger-tip-splitting phenomenon was found. It should be noted that we have verified that, if lower values of Ca are utilized, all the resulting weakly nonlinear interfaces look even more stable (almost circular in shape).

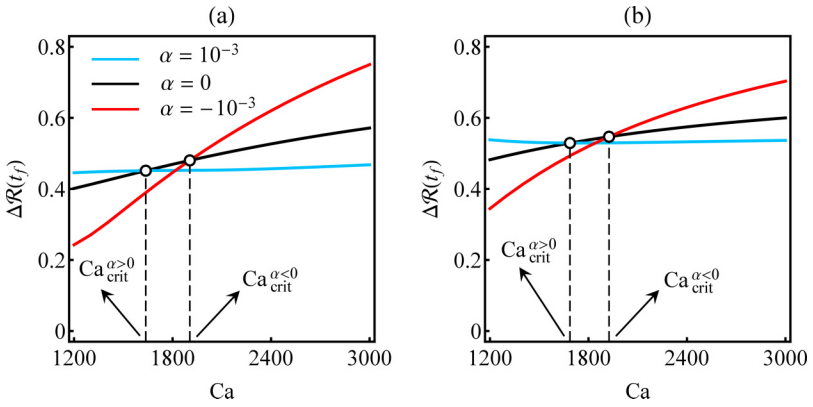

FIG. 5. Determination of the critical values of the capillary number at which the relative instability transitions. This is done by plotting the variation of finger length evaluated at final time $t = t_f$, $\Delta\mathcal{R}(t_f)$ as Ca is increased for $\alpha = -10^{-3}$, $\alpha = 0$, and $\alpha = 10^{-3}$. The critical capillary number $\mathrm{Ca}_{\mathrm{crit}}^{\alpha>0}$ ($\mathrm{Ca}_{\mathrm{crit}}^{\alpha<0}$) is determined by the point at which the curves for $\alpha = 0$ and $\alpha > 0$ ($\alpha < 0$) cross one another, as indicated by the vertical dashed lines. Here all physical parameters and initial conditions are identical to those utilized in (a) Fig. 3 [$n = 5$, $a_n(0) = 10^{-2}$, and $t_f = 13$], and (b) Fig. 6 [$n = 4$, $a_n(0) = 2.5 \times 10^{-2}$, and $t_f = 12$].

The visually based conclusions on the interface behavior discussed in the previous paragraph are fully substantiated by the more quantitative results presented in the bottom panel of Fig. 3(a) which plots the time evolution of the finger length $\Delta\mathcal{R}$ for the three values of α considered in the top panel. It is found that the $\Delta\mathcal{R}$ curve for $\alpha = -10^{-3}$ ($\alpha = 10^{-3}$) is indeed located below (above) the corresponding $\Delta\mathcal{R}$ curve for $\alpha = 0$. Since the quantity $\Delta\mathcal{R}$ is a measure of the finger perturbation amplitude, this means that the $\alpha < 0$ ($\alpha > 0$) interface is indeed relatively more stable (unstable) than the $\alpha = 0$ interface. As our theory is based on a first-order expansion in the rescaled slope $\alpha R/b_i$, at first glance one could expect that the distance between the $\Delta\mathcal{R}$ curve for $\alpha > 0$ and $\alpha = 0$ should be the same as the distance between the result for $\alpha < 0$ and $\alpha = 0$. However, this is not true since both b_i [see Eq. (3)] and R [see Eq. (5)] depend on α, such that higher-order effects on α come into play, introducing an asymmetry in the $\Delta\mathcal{R}$ curves plotted in the bottom panel of Fig. 3(a). This remark is also valid for the curves appearing in Figs. 3(b)–3(d), as well as in Fig. 6.

If one increases the value of Ca as illustrated in Fig. 3 and inspects the responses of the emerging interfaces, one detects that the strong stabilization provided by the converging cell in Fig. 3(a) becomes less and less effective. On the other hand, the more unstable diverging cell interfaces observed for lower Ca tend to become more and more stable (as compared with the parallel-plane ones) as the value of Ca is raised. Therefore, as Ca is increased, one eventually reaches a critical value of Ca [situation depicted in Fig. 3(b) where $\mathrm{Ca} = \mathrm{Ca}_{\mathrm{crit}} = \mathrm{Ca}_{\mathrm{crit}}^{\alpha>0} = 1637$] beyond which the relative stability behavior of the $\alpha > 0$ (diverging) interface with respect to the $\alpha = 0$ interface changes. In other words, if $\mathrm{Ca} > \mathrm{Ca}_{\mathrm{crit}}^{\alpha>0}$ the diverging interface will now be more stable than its uniform interface counterpart. These issues can be verified in Fig. 3(b), particularly in the bottom panel, where one can see that the $\Delta\mathcal{R}$ curves for $\alpha = 0$ and $\alpha > 0$ are nearly overlapping, and touch one another at $t = t_f$. Complementary information about this transitional behavior for diverging cells is given in Fig. 5(a), which describes how the finger length evaluated at time $t = t_f = 13$ [$\Delta\mathcal{R}(t_f)$] varies as Ca is increased. It is apparent from Fig. 5(a) that the curves for $\alpha = 0$ and $\alpha > 0$ cross each other at $\mathrm{Ca} = \mathrm{Ca}_{\mathrm{crit}}^{\alpha>0} = 1637$ [as indicated by the dashed vertical line on the left in Fig. 5(a)], in such a way that if $\mathrm{Ca} < \mathrm{Ca}_{\mathrm{crit}}^{\alpha>0}$ the diverging cell interface is more unstable than the uniform interface. In contrast, if $\mathrm{Ca} > \mathrm{Ca}_{\mathrm{crit}}^{\alpha>0}$ the diverging cell interface becomes more stable than the uniform interface. So at $\mathrm{Ca} = \mathrm{Ca}_{\mathrm{crit}}^{\alpha>0} = 1637$ there is in fact a transition in fingering stability behavior of the system for diverging cells.

It is worth noting that despite the transition behavior for diverging Hele-Shaw cells described above, and illustrated in Fig. 3(b) and in Fig. 5(a), the converging interface appearing in Fig. 3(b) is still more stable than the uniform one, as was the case in Fig. 3(a). This can be confirmed by inspecting the bottom panel of Fig. 3(b), where the $\Delta\mathcal{R}$ curve for $\alpha < 0$ is still standing below the $\Delta\mathcal{R}$ curve for $\alpha = 0$. Therefore, the occurrence of an instability transition for the interface behavior in diverging cells does not imply the development of a simultaneous change for flow in converging Hele-Shaw cells. Notice that by increasing Ca from Figs. 3(a) to 3(b) one sees that the $\Delta\mathcal{R}$ curves for $\alpha > 0$ and $\alpha < 0$ get closer to the $\Delta\mathcal{R}$ curve for $\alpha = 0$, indicating that the destabilization (stabilization) provided by the diverging (converging) cell becomes less intense. Another interesting aspect revealed in Fig. 3(b) is the observation that, irrespective of the value and sign of α, the finger tips in Fig. 3(b) are a bit wider and flatter than the finger tips observed in the interfaces depicted in Fig. 3(a). So, one concludes that by increasing Ca one notices a tendency toward finger-tip broadening and flattening ($\alpha = 0$ and $\alpha > 0$ curves), and even the very onset of a tip-splitting process ($\alpha < 0$ curve). These weakly nonlinear results about the shape of the patterns are also in line with the related findings (i.e., production of patterns having flattened finger tips) obtained in Ref. [44] for a similar range of values of Ca.

It turns out that, if one continues to increase the magnitude of the capillary number, one discovers another relative instability transition, now involving the interface behaviors in converging and uniform cells. As already pointed out in the previous paragraph, as Ca increases, the converging interface becomes increasingly more unstable as compared to the correponding uniform interface situation. In this scenario, one ultimately reaches another critical value for the capillary number [see Fig. 3(c) for which $\mathrm{Ca} = \mathrm{Ca}_{\mathrm{crit}} = \mathrm{Ca}_{\mathrm{crit}}^{\alpha<0} = 1905$], beyond which the converging interface will be more unstable than the equivalent parallel-plate cell interface. This situation can be easily identified in the bottom panel of Fig. 3(c) where the $\Delta\mathcal{R}$ curves for $\alpha = 0$ and $\alpha < 0$ are almost indistinguishable. The determination of this second critical value for the capillary number is illustrated in Fig. 5(a) corresponding to the point at which the $\Delta\mathcal{R}(t_f)$ curves for $\alpha = 0$ and $\alpha < 0$ intersect one another [as identified by the dashed vertical line on the right in Fig. 5(a)]. This higher Ca behavior is visualized in the top panel of Fig. 3(c), where the converging interface reveals a pattern displaying mild finger-tip-splitting events. Once again, this weakly nonlinear prediction is in qualitative accordance with the patterns simulated in Ref. [44] for the high-Ca regime, in which finger-tip splitting is proliferating.

If one increases Ca beyond the value of the critical capillary for the transition involving the converging and the uniform interfaces [i.e., if $\mathrm{Ca} > \mathrm{Ca}_{\mathrm{crit}}^{\alpha<0} = 1905$ as in Fig. 3(d) for which $\mathrm{Ca} = 3000$], the destabilizing role of the converging cell keeps increasing, and more intense tip splitting phenomena are detected for the $\alpha < 0$ situation. Equivalently, one finds that for such large values of Ca the stabilizing role of the diverging cell is reinforced. This can be seen in the bottom panel of Fig. 3(d), where the $\Delta\mathcal{R}$ curve for $\alpha > 0$ ($\alpha < 0$) is now below (above) the $\Delta\mathcal{R}$ curve for $\alpha = 0$, notably for larger values of time. We have also investigated how the critical values of the capillary number obtained in the analysis of Figs. 3 and 5(a) are modified, if the values of n and t_f are kept fixed, and if the initial perturbation amplitude $a_n(0)$ is varied. Regarding this specific point, we have found that if $a_n(0)$ is decreased (increased) the value of $\mathrm{Ca}_{\mathrm{crit}}$ is raised (lowered). For example, in case of Fig. 3 our tests indicate that a 2% change in $a_n(0)$ [note that the variation in $a_n(0)$ cannot be very large, since here we want to hold t_f unchanged] leads to an averaged change of about 10% (5%) in $\mathrm{Ca}_{\mathrm{crit}}^{\alpha<0}$ ($\mathrm{Ca}_{\mathrm{crit}}^{\alpha>0}$). However, we have also verified that the general trend of the fingering instability transition unveiled in Fig. 3 is robust with such changes in $a_n(0)$. We stress that these findings are also true for the data connected to Fig. 6, where the development of the instability transition will be examined in another set of values of n, $a_n(0)$, t_f, and Ca.

From the analysis of Fig. 3 one can infer that our mode-coupling approach is able to capture the most prominent pattern-forming behaviors that arise when the capillary number is varied in radially tapered Hele-Shaw cells: while in converging geometry the interface response changes from stabilizing at low Ca to destabilizing at high Ca, in diverging geometry the interface varies from more unstable at low Ca to more stable in the high Ca regime. Even though this is reassuring, in

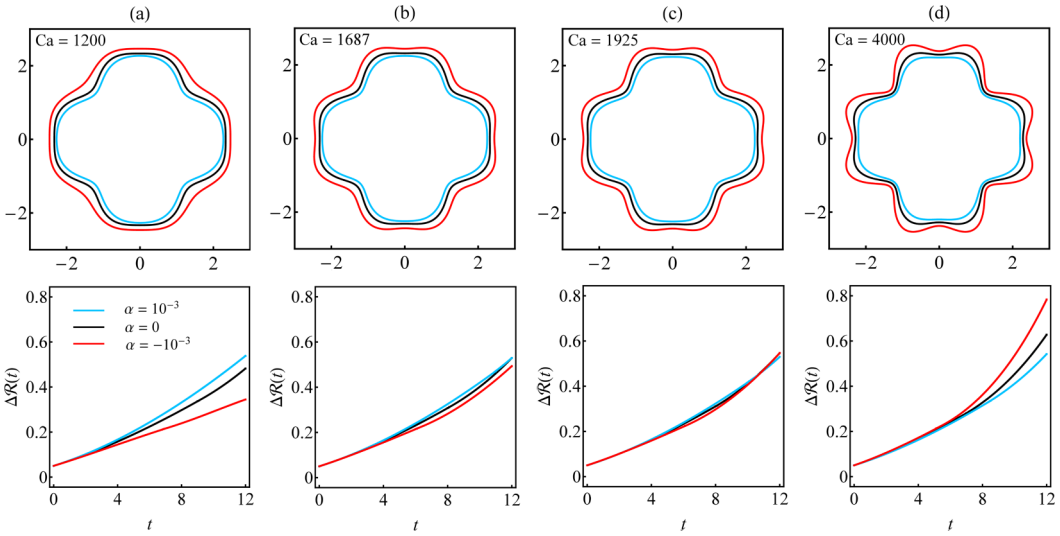

FIG. 6. Snapshot of the weakly nonlinear interfaces at time $t = t_f = 12$ (top panels), displaying characteristic fingering patterns for flow in diverging ($\alpha = 10^{-3}$), uniform ($\alpha = 0$), and converging ($\alpha = -10^{-3}$) Hele-Shaw cells. The following values of the capillary number are examined: (a) Ca = 1200, (b) Ca = 1687, (c) Ca = 1925, and (d) Ca = 4000. The interfaces are produced by taking into consideration the nonlinear coupling between modes n and $2n$, where $n = 4$. The corresponding time evolution of the finger length $\Delta\mathcal{R}(t)$ for $0 \leqslant t \leqslant t_f$ is depicted in the bottom panels.

order to strengthen the relevance of our weakly nonlinear results we revisit the situations examined in Fig. 3 by using a wider range of relevant parameters. Specifically, in Fig. 6 we investigate how the general trend uncovered in Fig. 3 regarding the instability transition is changed, if we consider different values for (1) the wave number n, (2) the initial amplitude $a_n(0)$, and (3) the final time t_f. While in Fig. 3 we analyzed the cases in which $n = 5$, $a_n(0) = 10^{-2}$, and $t_f = 13$, in Fig. 6 we examine the situation in which $n = 4$, $a_n(0) = 2.5 \times 10^{-2}$, and $t_f = 12$. By inspecting Figs. 3 and 6, comparing the interface responses to changes in Ca and the the related time evolution curves for finger length scale $\Delta\mathcal{R}(t)$, one verifies that despite the different values of n, $a_n(0)$, and t_f utilized in these plots, the general trend of the instability transition is detected. In addition to the situations studied in Figs. 3 and 6, we have also investigated two additional cases (figures not shown), for two more sets of parameters: (1) $n = 6$, $a_n(0) = 5.0 \times 10^{-3}$, and $t_f = 11$, and (2) $n = 3$, $a_n(0) = 5.5 \times 10^{-2}$, and $t_f = 15$. We stress that, also for these last two cases, we have encountered the same trends already found in Figs. 3 and 6.

Supplementary information about the transitional behaviors observed in Fig. 6 is given in Fig. 5(b). Of course, the values of the critical capillary numbers at which the relative instability behavior changes ($\mathrm{Ca_{crit}}$) are not the same in Fig. 3 [$\mathrm{Ca}_{\mathrm{crit}}^{\alpha>0} = 1637$, $\mathrm{Ca}_{\mathrm{crit}}^{\alpha<0} = 1905$] and Fig. 6 [$\mathrm{Ca}_{\mathrm{crit}}^{\alpha>0} = 1687$, $\mathrm{Ca}_{\mathrm{crit}}^{\alpha<0} = 1925$]. Likewise, other values of $\mathrm{Ca_{crit}}$ are found for the two additional sets of parameters mentioned in the previous paragraph, where in (1) we have $\mathrm{Ca}_{\mathrm{crit}}^{\alpha>0} = 1294$ and $\mathrm{Ca}_{\mathrm{crit}}^{\alpha<0} = 1928$, and in (2) we have $\mathrm{Ca}_{\mathrm{crit}}^{\alpha>0} = 2097$ and $\mathrm{Ca}_{\mathrm{crit}}^{\alpha<0} = 2317$. All this data indicate that the specific values for $\mathrm{Ca_{crit}}$ do depend on the parameters n, $a_n(0)$, and t_f. On the other hand, the dispersion in these values is not overly significant, pointing to the usefulness of our theoretical approach in describing the general features of the relative instability transition as n, $a_n(0)$, and t_f are modified. However, it should be clear that we are not claiming that the values of $\mathrm{Ca_{crit}}$ calculated for the situations illustrated in Figs. 3, 5, 6 and in the additional cases (1) and (2) are universal. Nevertheless, we can still say that the weakly nonlinear description is able to detect, and consistently mimic, the general trend of the fingering instability transition, and of the associated

finger morphological changes (finger-tip widening, flattening, and splitting) that emerge in radially tapered Hele-Shaw cell flows [44].

Various explanations for the stabilizing and destabilizing effects that emerge during fluid displacement in tapered Hele-Shaw cells have already been given in the literature [38–48]. In any case, at this point we present a brief discussion about the physical mechanisms responsible for changing the relative instability when the capillary number Ca is raised, as analyzed in the situations illustrated in Figs. 3 and 6. We begin with the converging geometry case, which involves the action of two stabilizing effects: the first one comes from the reduction of the transverse curvature $[\sim 1/b(r)]$. As the interface advances, $b(r)$ decreases in the direction of the flow, and the interface finds a region of higher transverse curvature that slows down the fingertips in comparison with parts of the interface which are further back in the cell plane. A second stabilizing effect is due to a decrease in the fluid mobility $[b(r)]^2/12\eta$ at the front of the interface. In opposition to these two stabilizing mechanisms, one has an increase in the viscous pressure gradient that tends to destabilize the interface. The competition among these three effects determines the relative instability discussed in Figs. 3 and 6. Under such circumstances, when lower Ca values are considered, the fluid mobility reduction and the increase of the transversal curvature dominate over the increase of the viscous effect. In this framing, the converging cell situation tends to be more stable than the parallel-plate case. On the other hand, as one increases Ca, the viscous pressure gradient overcomes the stabilizing contributions, and, thus, the converging gap leads to an increase in the formation of viscous fingers in comparison with the uniform Hele-Shaw cell case. Under the action of such stabilizing and destabilizing mechanisms, the interface responses are exactly reversed in the diverging geometry situation.

Earlier in this work, we have commented that, in general, one should not expect quantitative agreement between weakly nonlinear interface shapes and late-time pattern-forming structures obtained by intensive numerical simulations. We conclude our discussion in this section by addressing a closely related matter. More specifically, we justify why we have not provided a direct comparison between our weakly nonlinear interfaces, and the fully nonlinear ones obtained by the simulations performed in Ref. [44] for radially tapered Hele-Shaw cells. After all, one could wonder why we simply have not used the exact same set of parameters utilized in Ref. [44] and then tried to replicate their interface evolutions at least partially. This sounds quite reasonable and logical. In principle, to perform such a comparison, one could concentrate on situations presented in Ref. [44] in which the resulting interfaces are not excessively deformed, like the converging and uniform cell interfaces plotted in Fig. 6(a) of their paper.

Unfortunately, we have not succeeded in trying to reproduce some of the pattern-forming scenarios examined in Ref. [44]. Following Ref. [44], we used the parameters of their Fig. 6(a) [i.e., $\beta = 1250$, Ca $= 500$, $q = 100$, $\alpha = 0, \pm 10^{-3}$, $a_n(0) = 5.0 \times 10^{-2}$, $n = 8$, and time $t = 24$] to examine the time evolution of the equivalent weakly nonlinear shapes. It should be pointed out that the weakly nonlinear interfaces we generated were produced using all these parameters, with the exception of β. Since our theoretical model considers the infinite viscosity ratio limit ($\beta \to \infty$), we cannot take $\beta = 1250$ as in Ref. [44]. Regrettably, when we do all this and simulate the weakly nonlinear interfaces, we observed that the weakly nonlinear solutions "blow up" already at times considerably shorter than $t = 24$ (time used in Ref. [44] to plot their fully nonlinear interfaces). The resulting weakly nonlinear patterns presented very large amplitudes, revealing weird-looking interface shapes that show multiple self-intersections. The reason for this abnormal weakly nonlinear portrayal is the fact that, within the scope of our $\beta \to \infty$ model, both the initial amplitude $a_n(0)$ and the time ($t = 24$) utilized in Ref. [44] are so large, that under such circumstances the weakly nonlinear description is no longer valid. Of course, an important contributing factor for the disagreement between fully and weakly nonlinear interfaces is the fact that our $\beta \to \infty$ situation is even more unstable than the equivalent case studied in Ref. [44], in which β is large, but finite.

In closing, it should be clear that with the parameter choice made in Ref. [44], it is not plausible to directly contrast our modestly perturbed interfaces with their more complex, late-time structures.

Consequently, we could not make a direct comparison between the fully nonlinear interfaces obtained in Ref. [44], and the equivalent weakly nonlinear shapes produced by our perturbative mode-coupling scheme. By the way, this is the reason why, while plotting the various representative interfaces shown throughout this work, we had to consider sets of parameters distinct from that studied in Ref. [44]. In particular, for our $\beta \to \infty$ model, we had to use smaller values for the final times $t = t_f$. Moreover, in order to better illustrate the instability transition issues, and the related pattern-forming changes, we had to select proper values for the wave numbers n to ensure the validity of our weakly nonlinear perturbative approach.

IV. CONCLUSION

Our mode-coupling, weakly nonlinear results reveal that by increasing the value of the capillary number for viscous flows in radially tapered (slightly converging, or smoothly diverging) Hele-Shaw cells, one induces changes in the interface instability behavior relative to the corresponding interface response in a uniform (parallel-plate) Hele-Shaw cell. We have perceived that at lower Ca the converging cell interface is stabilized in comparison to the uniform cell interface, while at higher Ca the converging interface is relatively destabilized. Interestingly, these effects are exactly reversed in the diverging cell cases, where one finds more unstable interfaces in the low-Ca regime, and more stable interfacial feedback in the high-Ca regime. We have also been able to investigate how the overall shape of the emerging fingers is modified as Ca is increased: for both converging and diverging cell situations we observed that the finger tips are initially rounded for lower Ca, then get flattened at intermediate values of Ca, and finally tend to split at higher Ca.

It should be pointed out that our theoretical findings are qualitatively consistent with similar types of results obtained in Ref. [44] through intensive numerical simulations. This substantiates the usefulness and validity of our lowest nonlinear-order, perturbative mode-coupling approach in getting useful insights into the late-time pattern formation dynamics.

To conclude, it is worthwhile to note that a detailed experimental exploration of such a rich radially tapered Hele-Shaw cell system still needs to be developed in order to shed further light on the impact of the capillary number on the relative stability, and finger shape transitions theoretically scrutinized in this work and in Ref. [44].

ACKNOWLEDGMENTS

J.A.M. thanks CNPq (Brazilian Research Council) for financial support through Grant No. 304821/2015-2. E.O.D. acknowledges financial support from FACEPE through PPP Project No. APQ-0800-1.05/14. We are grateful to the authors of Ref. [44] for kindly supplying the numerical data of their Fig. 6(a). This paper has benefited from useful discussions with Rodolfo Brandão.

[1] P. G. Saffman and G. I. Taylor, The penetration of a fluid into a porous medium or Hele-Shaw cell containing a more viscous liquid, Proc. R. Soc. London Ser. A **245**, 312 (1958).

[2] P. Pelcé, *Dynamics of Curved Fronts* (Academic Press, New York, 1988).

[3] D. Kessler, J. Koplik, and H. Levine, Patterned selection in fingered growth phenomena, Adv. Phys. **37**, 255 (1988).

[4] For review papers see, for instance, G. M. Homsy, Viscous fingering in porous media, Annu. Rev. Fluid Mech. **19**, 271 (1987); K. V. McCloud and J. V. Maher, Experimental perturbations to Saffman-Taylor flow, Phys. Rep. **260**, 139 (1995); J. Casademunt, Viscous fingering as a paradigm of interfacial pattern formation: Recent results and new challenges, Chaos **14**, 809 (2004).

[5] P. G. Saffman, Viscous fingering in Hele-Shaw cells, J. Fluid Mech. **173**, 73 (1986).

[6] G. Tryggvason and H. Aref, Numerical experiments on Hele-Shaw flow with a sharp interface, J. Fluid Mech. **136**, 1 (1983).
[7] D. Bensimon, L. P. Kadanoff, S. Liang, B. I. Shraiman, and C. Tang, Viscous flow in two dimensions, Rev. Mod. Phys. **58**, 977 (1986).
[8] J. A. Miranda and M. Widom, Weakly nonlinear investigation of the Saffman-Taylor problem in a rectangular Hele-Shaw cell, Int. J. Mod. Phys. B **12**, 931 (1998).
[9] L. Paterson, Radial fingering in a Hele-Shaw cell, J. Fluid Mech. **113**, 513 (1981).
[10] J. D. Chen, Growth of radial viscous fingers in a Hele-Shaw cell, J. Fluid Mech. **201**, 223 (1989).
[11] J. A. Miranda and M. Widom, Radial fingering in a Hele-Shaw cell: A weakly nonlinear analysis, Physica D **120**, 315 (1998).
[12] I. Bischofberger, R. Ramanchandran, and S. R. Nagel, An island of stability in a sea of fingers: Emergent global features of the viscous-flow instability, Soft Matter **11**, 7428 (2015).
[13] J. E. Sader, D. Y. C. Chan, and B. D. Hughes, Non-Newtonian effects on immiscible viscous fingering in a radial Hele-Shaw cell, Phys. Rev. E **49**, 420 (1994).
[14] L. Kondic, M. J. Shelley, and P. Palffy-Muhoray, Non-Newtonian Hele-Shaw flow and the Saffman-Taylor Instability, Phys. Rev. Lett. **80**, 1433 (1998).
[15] A. Eslami and S. M. Taghavi, Viscous fingering regimes in elasto-visco-plastic fluids, J. Non-Newt. Fluid Mech. **243**, 79 (2017).
[16] C. T. Tan and G. M. Homsy, Simulation of nonlinear viscous fingering in miscible displacement, Phys. Fluids **31**, 1330 (1988).
[17] C.-Y. Chen and E. Meiburg, Miscible porous media displacements in the quarter five-spot configuration. Part 1. The homogeneous case, J. Fluid Mech. **371**, 233 (1998).
[18] B. Jha, L. Cueto-Felgueroso, and R. Juanes, Fluid Mixing from Viscous Fingering, Phys. Rev. Lett. **106**, 194502 (2011).
[19] T. Podgorski, M. C. Sostarecz, S. Zorman, and A. Belmonte, Fingering instabilities of a reactive micellar interface, Phys. Rev. E **76**, 016202 (2007).
[20] Y. Nagatsu, Viscous fingering phenomena with chemical reactions, Curr. Phys. Chem. **5**, 52 (2015).
[21] M. Zhao, A. Belmonte, S. Li, X. Li, and J. S. Lowengrub, Nonlinear simulations of elastic fingering in a Hele-Shaw cell, J. Comput. Appl. Math. **307**, 394 (2016).
[22] A. O. Tsebers and M. M. Maiorov, Magnetostatic instabilities in plane layers of magnetizable liquids, Magnetohydrodynamics (NY) **16**, 21 (1980).
[23] D. P. Jackson, R. E. Goldstein, and A. O. Cebers, Hydrodynamics of fingering instabilities in dipolar fluids, Phys. Rev. E **50**, 298 (1994).
[24] J. Kent-Dobias and A. J. Bernoff, Energy-driven pattern formation in planar dipole-dipole systems in the presence of weak noise, Phys. Rev. E **91**, 032919 (2015).
[25] L. W. Schwartz, Instability and fingering in a rotating Hele-Shaw cell or porous medium, Phys. Fluids A **1**, 167 (1989).
[26] L. Carrillo, F. X. Magdaleno, J. Casademunt, and J. Ortín, Experiments in a rotating Hele-Shaw cell, Phys. Rev. E **54**, 6260 (1996).
[27] E. Alvarez-Lacalle, J. Ortín, and J. Casademunt, Low viscosity contrast fingering in a rotating Hele-Shaw cell, Phys. Fluids **16**, 908 (2004).
[28] C.-Y. Chen, Y.-S. Huang, and J. A. Miranda, Diffuse-interface approach to rotating Hele-Shaw flows, Phys. Rev. E **84**, 046302 (2011).
[29] C. Ruyer-Quil, Inertial corrections to the Darcy law in a Hele-Shaw cell, C. R. Acad. Sci. II B **329**, 337 (2001).
[30] C. Chevalier, M. Ben Amar, D. Bonn, and A. Lindner, Inertial effects on Saffman-Taylor viscous fingering, J. Fluid Mech. **552**, 83 (2006).
[31] E. O. Dias and J. A. Miranda, Influence of inertia on viscous fingering patterns: Rectangular and radial flows, Phys. Rev. E **83**, 066312 (2011).
[32] C.-W. Park and G. M. Homsy, Two-phase displacement in Hele Shaw cells: Theory, J. Fluid Mech. **139**, 291 (1984).

[33] D. A. Reinelt and P. G. Saffman, The penetration of a finger into a viscous fluid in a channel and tube, SIAM J. Sci. Stat. Comp. **6**, 542 (1985).
[34] S. J. Jackson, D. Stevens, D. Giddings, and H. Power, Dynamic-wetting effects in finite-mobility-ratio Hele-Shaw flow, Phys. Rev. E **92**, 023021 (2015).
[35] H. Zhao and J. V. Maher, Viscous fingering experiments with periodic boundary conditions, Phys. Rev. A **42**, 5894 (1990).
[36] F. Parisio, F. Moraes, J. A. Miranda, and M. Widom, Saffman-Taylor problem on a sphere, Phys. Rev. E **63**, 036307 (2001).
[37] H. Aharoni, J. M. Kolinski, M. Moshe, I. Meirzada, and E. Sharon, Internal Stresses Lead to Net Forces and Torques on Extended Elastic Bodies, Phys. Rev. Lett. **117**, 124101 (2016).
[38] H. Zhao, J. Casademunt, C. Yeung, and J. V. Maher, Perturbing Hele-Shaw flow with a small gap gradient, Phys. Rev. A **45**, 2455 (1992).
[39] E. O. Dias and J. A. Miranda, Finger tip behavior in small gap gradient Hele-Shaw flows, Phys. Rev. E **82**, 056319 (2010).
[40] T. T. Al-Housseiny, P. A. Tsai, and H. A. Stone, Control of interfacial instabilities using flow geometry, Nat. Phys. **8**, 747 (2012).
[41] A. Juel, Fluid dynamics: Flattened fingers, Nat. Phys. **8**, 706 (2012).
[42] R. M. Wilson, Flow geometry controls viscous fingering, Phys. Today **65**(10), 15 (2012).
[43] T. T. Al-Housseiny and H. A. Stone, Controlling viscous fingering in tapered Hele-Shaw cells, Phys. Fluids **25**, 092102 (2013).
[44] S. J. Jackson, H. Power, D. Giddings, and D. Stevens, The stability of immiscible viscous fingering in Hele-Shaw cells with spatially varying permeability, Comput. Methods Appl. Mech. Eng. **320**, 606 (2017).
[45] T. Maxworthy, The effect of a stabilising gradient on interface morphology, in *Interfaces for the 21st Century: New Research Directions in Fluid Mechanics and Materials Science*, edited by M. K. Smith, M. J. Miksis, G. B. McFadden, G. P. Neitzel, and D. R. Canright (Imperial College Press, London, 2002), pp. 3–20.
[46] G. Bongrand and P. A. Tsai, Manipulation of viscous fingering in a radially tapered cell geometry, Phys. Rev. E **97**, 061101(R) (2018).
[47] D. Pihler-Puzović, P. Illien, M. Heil, and A. Juel, Suppression of Complex Fingerlike Patterns at the Interface between Air and a Viscous Fluid by Elastic Membranes, Phys. Rev. Lett. **108**, 074502 (2012).
[48] D. Pihler-Puzović, G. G. Peng, J. R. Lister, M. Heil, and A. Juel, Viscous fingering in radial elastic-walled Hele-Shaw cell, J. Fluid Mech. **849**, 163 (2018).
[49] S.-Z. Zhang, E. Louis, O. Pla, and F. Guinea, Linear stability analysis of the Hele-Shaw cell with lifting plates, Eur. Phys. J. B **1**, 123 (1998).
[50] S. Hassani, *Mathematical Physics: A Modern Introduction to Its Foundations* (Springer-Verlag, New York, 1999).
[51] H. Guo, D. C. Hong, and D. A. Kurtze, Surface-Tension-Driven Nonlinear Instability in Viscous Fingers, Phys. Rev. Lett. **69**, 1520 (1992).
[52] H. Guo, D. C. Hong, and D. A. Kurtze, Dynamics of viscous fingers and threshold instability, Phys. Rev. E **51**, 4469 (1995).
[53] E. Alvarez-Lacalle, J. Casademunt, and J. Ortín, Systematic weakly nonlinear analysis of interfacial instabilities in Hele-Shaw flows, Phys. Rev. E **64**, 016302 (2001).
[54] E. Alvarez-Lacalle, E. Pauné, J. Casademunt, and J. Ortín, Systematic weakly nonlinear analysis of radial viscous fingering, Phys. Rev. E **68**, 026308 (2003).
[55] L. N. Brush and R. F. Sekerka, A numerical study of two-dimensional crystal growth forms in the presence of anisotropic growth kinetics, J. Crystal Growth **96**, 419 (1989).
[56] M. J. P. Gingras and Z. Rácz, Noise and the linear stability analysis of viscous fingering, Phys. Rev. A **40**, 5960 (1989).
[57] P. Fast and M. J. Shelley, Moore's law and the Saffman-Taylor instability, J. Comput. Phys. **212**, 1 (2006).
[58] J. Mathiesen, I. Procaccia, H. L. Swinney, and M. Thrasher, The universality class of diffusion-limited aggregation and viscous fingering, Europhys. Lett. **76**, 257 (2006).

[59] S. W. Li, J. S. Lowengrub, J. Fontana, and P. Palffy-Muhoray, Control of Viscous Fingering Patterns in a Radial Hele-Shaw Cell, Phys. Rev. Lett. **102**, 174501 (2009).

[60] S. J. Jackson, D. Stevens, H. Power, and D. Giddings, A boundary element method for the solution of finite mobility ratio immiscible displacement in a Hele-Shaw cell, Int. J. Numer. Methods Fluids **78**, 521 (2015).

[61] P. H. A. Anjos, E. O. Dias, and J. A. Miranda, Radial fingering under arbitrary viscosity and density ratios, Phys. Rev. Fluids **2**, 084004 (2017).